Scattering From Multiple Objects Buried Beneath Two-Dimensional Random Rough Surface Using the Steepest Descent Fast Multipole Method

Magda El-Shenawee, *Senior Member, IEEE*

***Abstract*—Generalized formulations are presented to analyze the electric field scattered from multiple penetrable shallow objects buried beneath two-dimensional random rough surfaces. These objects could have different materials, shapes, or orientations. In addition, their separation distance may range from a fraction of a wavelength to several wavelengths. The fast algorithm, steepest descent fast multipole method (SDFMM), is used to compute the unknown electric and magnetic surface currents on the rough ground surface and on the buried objects. Parametric investigations are presented to study the effect of the objects proximity, orientations, materials, shapes, the incident waves polarization, and the ground roughness on the scattered fields. A significant interference is observed between the objects when they are separated by less than one free space wavelength. Even when the clutter due to the rough ground is removed, the return from the second object, can be dominating causing a possible false alarm in detecting the target. The results show that the distortion in target signature significantly increases with the increase of both the proximity to a clutter item and the ground roughness.**

***Index Terms*—Computational electromagnetics, multiple objects, rough surface scattering, steepest descent fast multipole method (SDFMM), subsurface sensing.**

I. Introduction

SEVERAL research works, in the frequency and in the time domain, have been published in the area of sensing objects buried under or above the Earth's surface. Some of the published work is related to objects buried in random media to simulate the clutter (no presence of a rough or planar interface) [1]. In other work, the air–ground interface has been ignored justified by the very nearby position of the transmitting/receiving antennas to the ground [2], and in other several publications the roughness of the Earth's surface has been ignored by assuming a planar half space, where the objects are either buried under the interface [3]–[6], partially immersed in a semi-infinite dielectric medium [7] or located above the half space [8]. Radar images for targets buried under planar and or rough ground are published in [9]–[11]. It is known that the roughness of the ground is a major source of clutter for target detection, however, due to its complicated analysis, several researchers have assumed that the interface is rough only in one-dimension (1-D) [i.e., two-dimension (2-D) scattering problem] [12]–[16] where there was either a perfectly electric conducting (PEC) or a penetrable (dielectric) cylindrical target buried under the rough interface. In reality, the Earth's surface is rough in 2-D, which added more complexity to the analysis of the problem as in [17] where the buried target is a PEC sphere, in [18] and [19] where the object is located above the interface, and in [20] and [21] where the buried target is a penetrable and/or PEC spheroid. Recent experimental work is conducted to discriminate landmines from various clutter items using electromagnetic induction (EMI) [22]. Even though [22] focused on using the EMI, however, investigating the influence of clutter items on the target signature is necessary, which is the motivation of this work. The emphasis in this paper will be on sensing two dielectric objects buried under a two-dimensional random rough ground as shown in Fig. 1. To the best of our knowledge, this application has not been analyzed before due its excessive computational requirements. Therefore, the SDFMM, [23]–[25], is modified for this application to make these computations tractable. The mathematical formulations are derived in Section II, numerical results are presented in Section III and concluding remarks are given in Section IV.

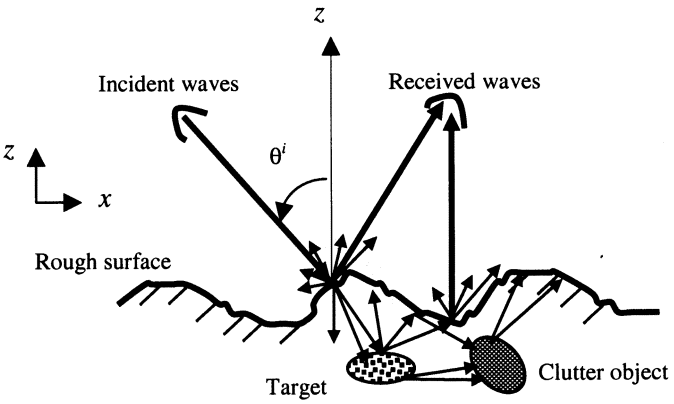

Fig. 1. Cross section of two penetrable objects buried beneath the rough surface ground.

II. Formulation

The equivalence theorem is applied to express the electric and the magnetic fields as functions of electric and magnetic surface currents. As depicted in Fig. 2(a), the permittivity and permeability in region R_j are given by ε_j and μ_j, respectively, where $j = 1, 2, \cdots, K_r$ where K_r is the total number of regions (e.g., $K_r = 4$ in Fig. 1). The surface boundary $S_{j,n}$ is separating regions R_j and R_n, where $n = 1, 2, \cdots, K_r$, $n \neq j$ (e.g. for

Manuscript received June 22, 2001; revised February 13, 2002. This work was supported by Northeastern University Demining MURI Grant No. DAA 0-55-97-0013.

The author is with the Department of Electrical Engineering, University of Arkansas, Fayetteville, AR 72701 USA (magda@uark.edu).

Digital Object Identifier 10.1109/TAP.2003.811096

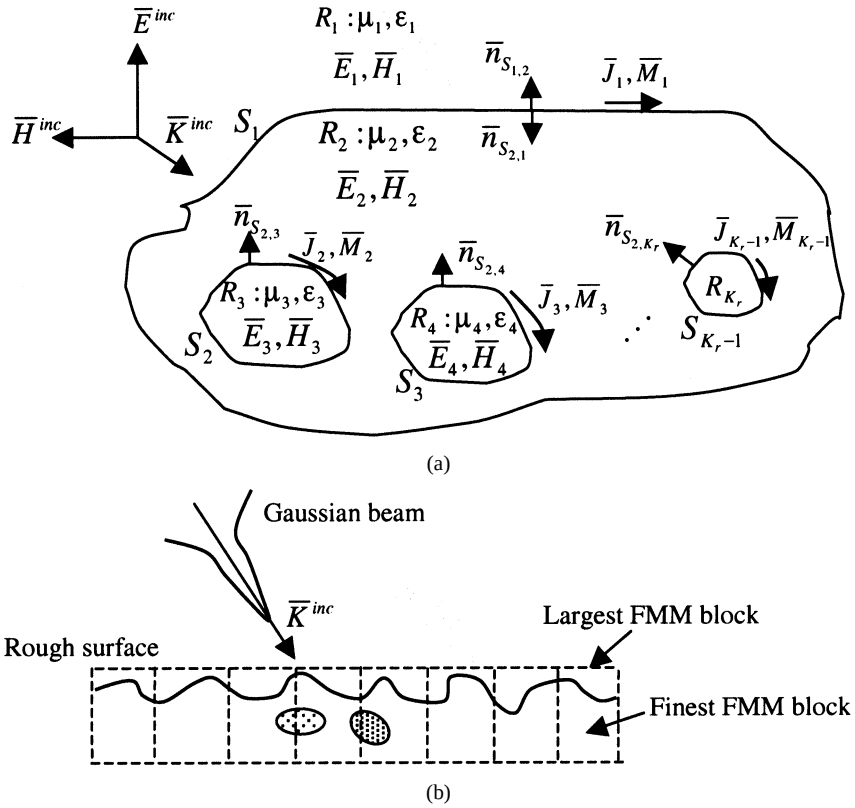

Fig. 2. (a) General penetrable 3-D scatterers, $R_2, R_3, \ldots, R_{K_r-1}$. (b) Pictorial description of the SDFMM showing the fast multiple method (FMM) blocks.

$K_r = 4$, $S_{1,2} = S_{2,1} = S_1$, $S_{2,3} = S_{3,2} = S_2$ and $S_{2,4} = S_{4,2} = S_3$). Note that $S_{j,n}$ does not exist if regions R_j and R_n do not have common boundary. The unit vector $\overline{n}_{S_{j,n}}$ is normal to the surface $S_{j,n}$ pointing into the region R_j as shown in Fig. 2(a) with $\overline{n}_{S_{j,n}} = -\overline{n}_{S_{n,j}}$. Assuming time dependence of $\exp(i\omega t)$, the general forms of the electric and magnetic fields $\overline{E}_j$ and $\overline{H}_j$, respectively, at an arbitrary point $\overline{r}$ in region R_j are [20] and [26]

$$\begin{aligned}\theta_j(\overline{r})\overline{E}_j(\overline{r}) = {} & \overline{E}_j^{inc}(\overline{r}) - \sum_{\substack{n=1\\ n\neq j}}^{K_r} \int_{S_{j,n}} \Big(i\omega\mu_j \left(\overline{n}_{S_{j,n}} \times \overline{H}_j\right) \Phi_j \\ & - \left(\overline{n}_{S_{j,n}} \times \overline{E}_j\right) \times \nabla'\Phi_j \\ & - \left(\overline{n}_{S_{j,n}} \cdot \overline{E}_j\right) \nabla'\Phi_j \Big)\, ds' \end{aligned} \tag{1a}$$

$$\begin{aligned}\theta_j(\overline{r})\overline{H}_j(\overline{r}) = {} & \overline{H}_j^{inc}(\overline{r}) + \sum_{\substack{n=1\\ n\neq j}}^{K_r} \int_{S_{j,n}} \Big(i\omega\varepsilon_j \left(\overline{n}_{S_{j,n}} \times \overline{E}_j\right) \Phi_j \\ & + \left(\overline{n}_{S_{j,n}} \times \overline{H}_j\right) \times \nabla'\Phi_j \\ & + \left(\overline{n}_{S_{j,n}} \cdot \overline{H}_j\right) \nabla'\Phi_j \Big)\, ds' \end{aligned} \tag{1b}$$

in which $i = \sqrt{-1}$, the symbol $\theta_j(\overline{r})$ is the Heaviside function at surface $S_{j,n}$ in region R_j. The three-dimensional (3-D) scalar Green's function is given by $\Phi_j = \exp(-ik_j|\overline{r}-\overline{r}'|)/4\pi|\overline{r}-\overline{r}'|$, where $\overline{r}'$ is the source point and $k_j = \omega\sqrt{\varepsilon_j\mu_j}$ is the wave number of region R_j. Note that in Fig. 2(a), $\overline{E}_j^{\text{inc}} = 0$ and $\overline{H}_j^{\text{inc}} = 0$ for $j = 2, 3, \cdots, K_r$. Applying the boundary conditions for the tangential electric and magnetic fields on surface $S_{l,n}$ with $l, n = 1, 2, 3, \cdots, K_r$, $l \neq n$ leads to the general electric and magnetic field equations

$$\begin{aligned}\overline{E}^{inc}(\overline{r})|_{\text{tang.}S_{l,n}} = {} & \sum_{l'=1}^{K_r} \Big[\Big(L_{S_{l,l'}} \overline{J}_{S_{l,l'}} - L_{S_{n,l'}} \overline{J}_{S_{n,l'}} \Big) \\ & - \Big(K_{S_{l,l'}} \overline{M}_{S_{l,l'}} - K_{S_{n,l'}} \overline{M}_{S_{n,l'}} \Big) \Big]_{\text{tang.}} \end{aligned} \tag{2a}$$

$$\begin{aligned}\overline{H}^{inc}(\overline{r})|_{\text{tang.}S_{l,n}} = {} & \sum_{l'=1}^{K_r} \Big[\Big(K_{S_{l,l'}} \overline{J}_{S_{l,l'}} - K_{S_{n,l'}} \overline{J}_{S_{n,l'}} \Big) \\ & + \Big(\frac{L_{S_{l,l'}}}{\eta_l^2} \overline{M}_{S_{l,l'}} - \frac{L_{S_{n,l'}}}{\eta_n^2} \overline{M}_{S_{n,l'}} \Big) \Big]_{\text{tang.}} \end{aligned} \tag{2b}$$

in which $\overline{J}_{S_{l,n}}$ and $\overline{M}_{S_{l,n}}$ are the unknown electric and magnetic surface currents on $S_{l,n}$, respectively, and $\eta_l = \sqrt{\mu_l/\varepsilon_l}$ is the intrinsic impedance in region R_l. Note that $\overline{J}_{S_{1,2}} = -\overline{J}_{S_{2,1}} = \overline{J}_1$, $\overline{J}_{S_{2,3}} = -\overline{J}_{S_{3,2}} = \overline{J}_2$, $\overline{J}_{S_{2,4}} = -\overline{J}_{S_{4,2}} = \overline{J}_3$ etc. The integro-differential operators $L_{S_{l,n}}$ and $K_{S_{l,n}}$ are given by

$$L_{S_{l,n}}\overline{X} = \int_{S_{l,n}} \left\{ i\omega\mu_l \Phi_l \overline{X}(\overline{r}') + \frac{i}{\omega\varepsilon_l} \nabla\nabla' \cdot \overline{X}(\overline{r}') \Phi_l \right\} ds'$$

and

$$K_{S_{l,n}}\overline{X} = \int_{S_{l,n}} \overline{X}(\overline{r}') \times \nabla\Phi_l ds' \tag{2c}$$

in which the vector $\overline{X}$ represents the surface current noting that $L_{S_{l,n}} \neq L_{S_{n,l}}$ and $K_{S_{l,n}} \neq K_{S_{n,l}}$. All surfaces are discretized

into triangular patches where the unknown currents in (2) are approximated using the Rao–Wilton–Glisson vector basis functions $\overline{j}(\overline{r})$ [27] as

$$\overline{J}_k(\overline{r}) = \sum_{n=1}^{N_k} I_n^{(k)} \overline{j}_n^{(k)}(\overline{r}), \quad \overline{M}_k(\overline{r}) = \eta_1 \sum_{n=1}^{N_k} I_{n+N_k}^{(k)} \overline{j}_n^{(k)}(\overline{r}) \quad \overline{r} \in S_k, \quad k = 1, 2, \ldots, K_r - 1 \tag{3}$$

in which N_k is the number of unknowns on scatterer S_k, and $I_n^{(k)}$ and $\overline{j}_n^{(k)}$ are the unknown coefficients and the vector basis function of edge n, respectively. Note that $S_{1,2} = S_{2,1} = S_1$, $S_{2,3} = S_{3,2} = S_2$, $S_{2,4} = S_{4,2} = S_3$, etc. Upon substituting (3) in (2), normalizing the H-field equations (2b) by η_1, and applying Galerkin's method for testing (2a) and (2b), the linear system of equations is obtained

$$\overline{\overline{Z}}\,\overline{I} = \overline{V}. \tag{4a}$$

The general expressions of the impedance matrix $\overline{\overline{Z}}$ for multiple scatterers immersed in R_2 in Fig. 2(a) is given by (4b) at the bottom of the page, where submatrix $\overline{Z}_{S_{n,l}}$ represents the interactions of elements on surface $S_{n,l}$ (self interactions) and $\langle \overline{A}, \overline{B} \rangle_S$ denotes the complex inner product between vector functions $\overline{A}$ and $\overline{B}$ on a surface S [20], [26]. The general expressions of the submatrix $\overline{Z}_{S_{n,l}S_{l,k}}$ which represent the interactions of elements on surface $S_{n,l}$ with elements on surface $S_{l,k}$ (mutual interactions), with $n, l, k = 1, 2, \cdots, K_r$, $n \neq l$, $k \neq l$ can be written as (4c) at the bottom of the page,where the term η_1 is used to normalize the H-equations in (2b) and the magnetic currents in (3). In (4a), the vector $\overline{I}$ includes all the unknown current coefficients in (3) and the vector $\overline{V}$ is the tested incident tangential electric and magnetic fields on the exterior surface of each scatterer.

Solving the system of (4) by using the method of moments (MoM) requires computing and storing the elements of the full dense matrix $\overline{\overline{Z}}$ and then multiplying it by the vector $\overline{V}$ leading to $O(K^2)$ computational complexity for the CPU time and computer memory. Therefore, the SDFMM is used in this work to reduce the computational complexity to only $O(K)$ per iteration [23], [24], where, the quantity $K = 2(N_1 + N_2 + \cdots + N_{K_r - 1})$ is the total number of the unknown coefficients in (3). Modifying the SDFMM for the current application is to basically enclose the whole scatterer (the rough surface and the buried objects) by a large block, which is further subdivided into smaller blocks as shown in Fig. 2(b). The elements of $\overline{\overline{Z}}$ that are due to interactions between edges located in the same fine block and/or in neighboring fine blocks are calculated and stored using the standard MoM (near-field interactions). These edges could be on the ground or on the surfaces of objects. On the other hand, when these edges are located in blocks that are far from each other, the corresponding $\overline{\overline{Z}}$ elements are not directly calculated or stored, leading to convert $\overline{\overline{Z}}$ into a sparse matrix (far-field interactions). However, the matrix-vector multiplication of these elements by the vector $\overline{I}$ is calculated in one step, as discussed in [23]–[25].

III. Numerical Results

In this section, numerical results are presented for two objects buried beneath the rough ground. A carefully tapered incident Gaussian beam is used for excitation to eliminate the effects of the artificial edges of the modeled ground [28]. Thus, the closed surface S_1, in Fig. 2(a), can be approximated by an open surface of dimensions $L \times L$. Several dimensions of the modeled ground are tested, however, the $8\lambda_0 \times 8\lambda_0$ dimensions are adopted since it simulates, at 1 GHz, the ground-penetrating radar (GPR) experiments presented in [29] and [30]. The half-beam width of the Gaussian beam is assumed to be $1.6\lambda_0$, which illuminates the ground with plane waves over a spot of diameter $3.2\lambda_0$ centered at $x = 4\lambda_0$, $y = 4\lambda_0$ (ground center). The rough ground surface is characterized with Gaussian statistics for the heights, assuming zero mean and root mean square (rms) σ, and for the autocorrelation function with correlation length l_c. The computer random generator is used to generate random numbers from Gaussian distribution, with the specified statistics, which are assigned to the heights (z-direction) of the surface nodes. These random numbers are correlated through the specified autocorrelation function [31]. The relative dielectric constant of the ground is assumed to be $\varepsilon_r = 2.5 - j0.18$ [32] while the dielectric constant of the objects will be stated for each case. The discretization distance on the ground surface is assumed to be $0.08\lambda_0$ leading to 60 000 electric and magnetic surface current unknowns $(2N_1)$, while using almost the same discretization rate for the two objects generates approximately 600 unknowns for each one $(2N_2, 2N_3)$.

$$\overline{Z}_{S_{n,l}} = \begin{pmatrix} \left\langle \overline{j}_{S_{n,l}}, \left(L_{S_{n,l}} + L_{S_{l,n}}\right) \overline{j}_{S_{n,l}} \right\rangle_{S_{n,l}} & \left\langle \overline{j}_{S_{n,l}}, -\eta_1 \left(K_{S_{n,l}} + K_{S_{l,n}}\right) \overline{j}_{S_{n,l}} \right\rangle_{S_{n,l}} \\ \left\langle \overline{j}_{S_{n,l}}, \eta_1 \left(K_{S_{n,l}} + K_{S_{l,n}}\right) \overline{j}_{S_{n,l}} \right\rangle_{S_{n,l}} & \left\langle \overline{j}_{S_{n,l}}, \eta_1^2 \left(\frac{L_{S_{n,l}}}{\eta_n^2} + \frac{L_{S_{l,n}}}{\eta_l^2}\right) \overline{j}_{S_{n,l}} \right\rangle_{S_{n,l}} \end{pmatrix} \tag{4b}$$

$$\overline{Z}_{S_{n,l}S_{l,k}} = \begin{pmatrix} \left\langle \overline{j}_{S_{n,l}}, -L_{S_{l,k}} \overline{j}_{S_{l,k}} \right\rangle_{S_{n,l}} & \left\langle \overline{j}_{S_{n,l}}, \eta_1 K_{S_{l,k}} \overline{j}_{S_{l,k}} \right\rangle_{S_{n,l}} \\ \left\langle \overline{j}_{S_{n,l}}, -\eta_1 K_{S_{l,k}} \overline{j}_{S_{l.k}} \right\rangle_{S_{n,l}} & \left\langle \overline{j}_{S_{n,l}}, -\eta_1^2 \frac{L_{S_{l,k}}}{\eta_l^2} \overline{j}_{S_{l,k}} \right\rangle_{S_{n,l}} \end{pmatrix} \tag{4c}$$

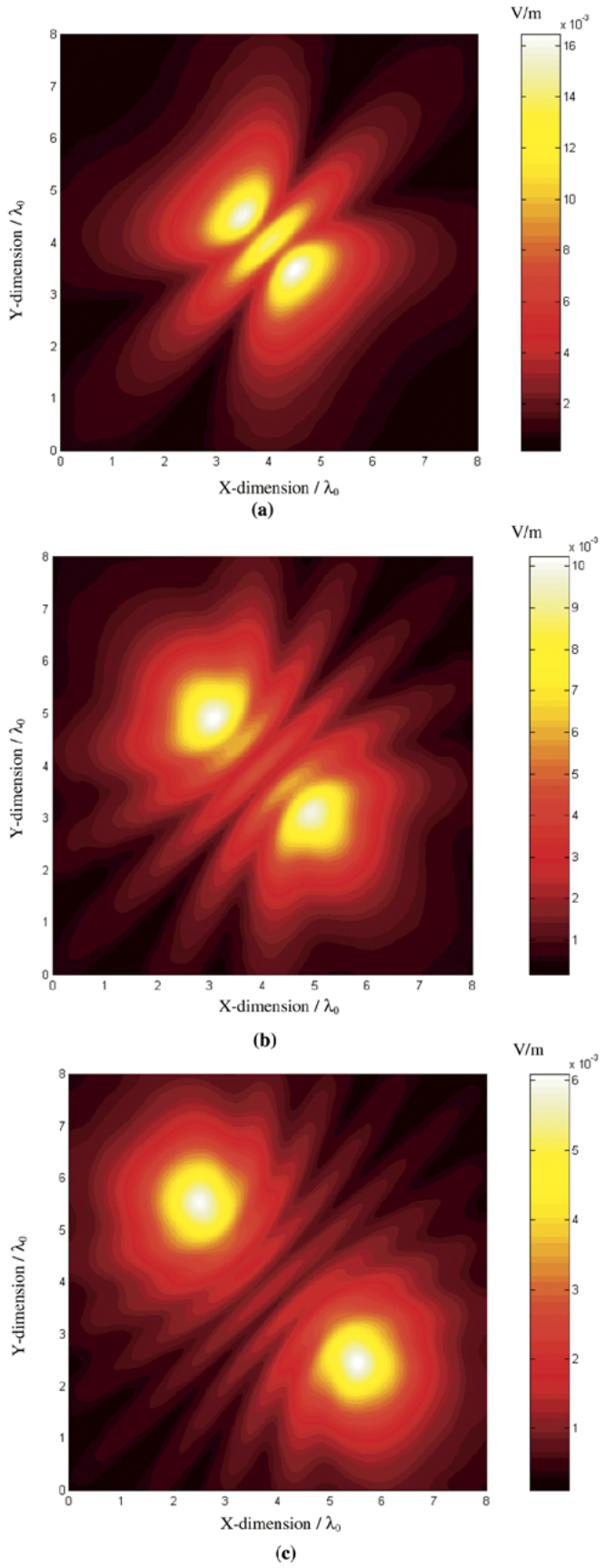

Fig. 3. Scattered electric field above a flat ground at $z = 0.5\lambda_0$ due to just the two penetrable spheroids with separating distance equal to (a) $D_x = D_y = 1\lambda_0$, (b) $D_x = D_y = 2\lambda_0$, (c) $D_x = D_y = 3\lambda_0$. H polarization.

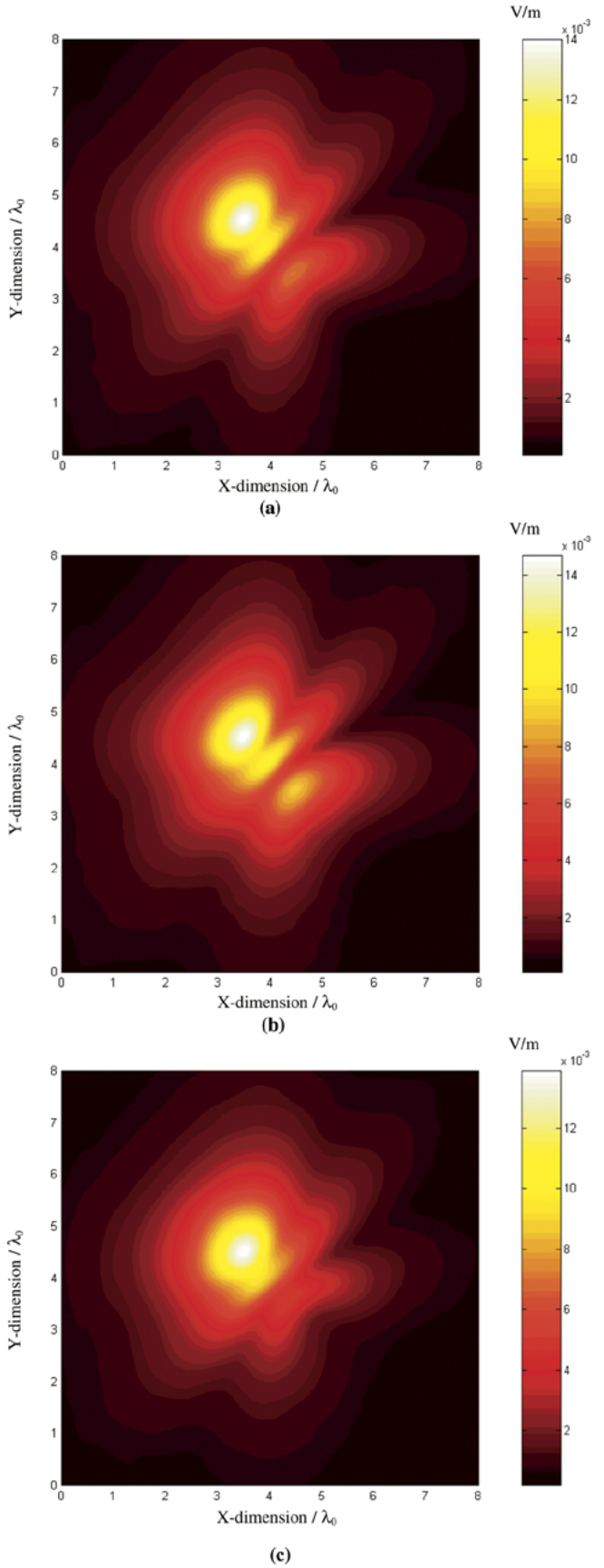

Fig. 4. Scattered electric field above a flat ground at $z = 0.5\lambda_0$ due to (a) the spheroid and the sphere, (b) the spheroid and the ellipsoid, and (c) the spheroid and the disk (vertical cylinder). The separation distance for (a)-(c) is $D_x = D_y = 1\lambda_0$. H polarization.

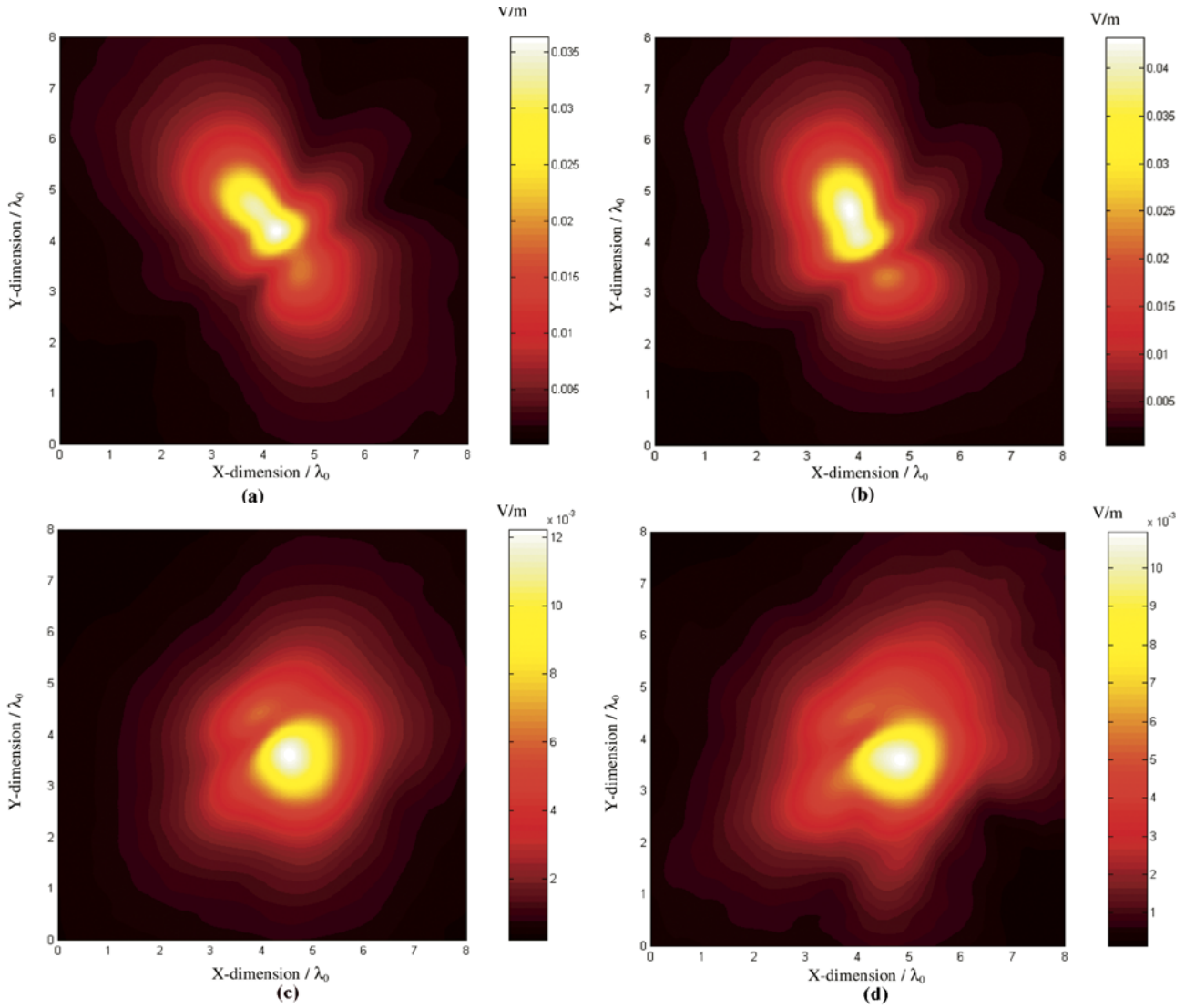

Fig. 5. Scattered electric field at $z = 0.5\lambda_0$ above the rough ground due to just (a) both the spheroid and the horizontal cylinder for $\sigma = 0.04\lambda_0$; H-polarization. (b) Both the spheroid and the horizontal cylinder for same data for V-polarization. (c) Spheroid alone for same data, H-polarization and (d) the spheroid alone for same data but for $\sigma = 0.1\lambda_0$, H-polarization. All results are for $D_x = 0.49\lambda_0$, $D_y = 0.875\lambda_0$, and $l_c = 0.5\lambda_0$.

Images based on the magnitude of the scattered electric fields from the two buried objects will be presented. The electric fields are received at $z = 0.5\lambda_0$ above the mean plane of the rough ground with $0.04\lambda_0$ for resolution [33]. In Figs. 3 and 4, the ground is assumed to be flat in order to investigate the clutter due to only the second object (i.e., without the rough ground). The scattered fields due to just the two objects are obtained by subtracting the ground returns from the returns from the ground with buried objects in complex vector representation. The SDFMM was validated with the MoM using small-scale cases. The parametric investigation in this section includes studying the effect on the scattered fields due to 1) proximity between the two objects, 2) their materials, 3) shapes, 4) orientations, 5) incidence polarization, and 6) ground roughness. The images shown in Fig. 3(a)–(c) are for two oblate spheroids with dimensions $a = 0.15\lambda_0$, $b = 0.3\lambda_0$, material of $\varepsilon_r = 2.9 - j0.072$, and buried at $z = -0.3\lambda_0$. They are located diagonally at $x = 4.5\lambda_0$, $y = 3.5\lambda_0$ and $x = 3.5\lambda_0$, $y = 4.5\lambda_0$ in Fig. 3(a), at $x = 5\lambda_0$, $y = 3\lambda_0$ and $x = 3\lambda_0$, $y = 5\lambda_0$ in Fig. 3(b), and at $x = 5.5\lambda_0$, $y = 2.5\lambda_0$ and $x = 2.5\lambda_0$, $y = 5.5\lambda_0$ in Fig. 3(c). This implies that the separation distance from the center of the first object to the center of the second object is $D_x = D_y = 1\lambda_0$, $2\lambda_0$ and $3\lambda_0$ in Fig. 3(a)–(c), respectively, where D_x and D_y are the distances in the x- and y-direction, respectively. A significant interference between the two objects is observed in Fig. 3(a) where the separation distance is $D_x = D_y = 1\lambda_0$. This coupling between the two objects decreases with the increase of the D_x and D_y as shown in Fig. 3(b) and (c). The results show that when the objects are separated by $3\lambda_0$ or more, each object can be detected individually (e.g., by narrowing the width of the incident beam). Moreover, the results in Fig. 3(a)–(c) show the decrease of the signature magnitude when the objects are moved away from the center of the ground, where the incident beam is centered, which agrees with the results presented in [21].

In Fig. 4(a)–(c), the shape of the two objects are changed such that the spheroid is used for one object while the second

object is assumed to be a sphere of radius $a = 0.15\lambda_0$ in Fig. 4(a), an ellipsoid of dimensions $a = 0.15\lambda_0$, $b = 0.3\lambda_0$, $c = 0.15\lambda_0$ in Fig. 4(b), and a disk (vertical cylinder) of radius $a = 0.15\lambda_0$ and height $h = 0.15\lambda_0$ in Fig. 4(c). The two objects in Fig. 4(a)–(c) are located similar to those in Fig. 3(a) where $D_x = D_y = 1\lambda_0$. The scattered fields from just the spheroid and the sphere, the spheroid and the ellipsoid, and the spheroid and the disk are shown in Fig. 4(a)–(c). The results show that the signature of the spheroid (located in the upper left quadrant) is much larger than the signature of the sphere, ellipsoid or the disk (located in the lower right quadrant). However, the signature of the spheroid with the presence of the ellipsoid has slightly larger magnitude than the sphere or the disk. Because the two objects have different shapes and sizes, the interference between them is clearly not symmetric, contrary to the results of Fig. 3(a)–(c). In Figs. 3 and 4, both objects are assumed to have the same material $(\varepsilon_r = 2.9 - j0.072)$ and they are buried under a flat ground.

To simulate a more realistic case, different material for the second object will be assumed in addition to incorporating the ground roughness in the simulation as shown in Fig. 5(a)–(d). In this case, the spheroid is assumed to have the same material and dimensions as in Fig. 3 located at $x = 4.5\lambda_0$, $y = 3.5\lambda_0$, and $z = -0.3\lambda_0$ (i.e. in the lower right quadrant). The second object is assumed to be a horizontal cylinder of radius $a = 0.15\lambda_0$, height $h = 0.9\lambda_0$ with its axis tilted at angle 30° with the x-direction. The material of this horizontal cylinder is assumed to be lossless with $\varepsilon_r = 4$ (dry wood) and its center is located at $x = 4.01\lambda_0$, $y = 4.375\lambda_0$, and $z = -0.3\lambda_0$ (i.e. in the upper left quadrant), which implies that $D_x = 0.49\lambda_0$ and $D_y = 0.875\lambda_0$. The ground roughness are $\sigma = 0.04\lambda_0$ and $l_c = 0.5\lambda_0$. The results in Fig. 5(a) and (b) are for the incident H- and V-polarizations, respectively. These results show that the signature of the horizontal cylinder is dominating the image with maximum magnitude of almost three times larger than the spheroid. This is due to the larger size and dielectric constant of the cylinder in addition to its tilted position with the x-direction. Upon comparing Fig. 5(a) with (b), a polarization dependence is clearly observed with slight increase in the maximum magnitude for the V-polarization case in Fig. 5(b). Moreover, the results in Fig. 5(a) and (b) indicate that the presence of the clutter item (cylinder) can easily cause a false alarm in detecting the target (spheroid) for both polarizations. To analyze the signature of the spheroid alone, all sources of clutter are approximately removed. This procedure implies running the computer code twice; one time to compute the scattered fields from the rough ground with the buried cylinder and a second time to compute the scattered fields from the rough ground with both the buried cylinder and spheroid. These fields are subtracted and the output represents the scattered fields from just the spheroid, in addition to noise due to the interferences with the cylinder and the rough ground. The results are plotted in Fig. (c) for the H-polarization case and similar results are observed for the V-polarization case (not presented). In Fig. 5(d), the signature of the spheroid is plotted for rougher ground surface where $\sigma = 0.1\lambda_0$ using the same data of Fig. 5(a) but with burial depth equal to $z = -0.4\lambda_0$. Comparing Fig. 5(d) with (c), it is clear that increasing the ground roughness has increased the distortion level

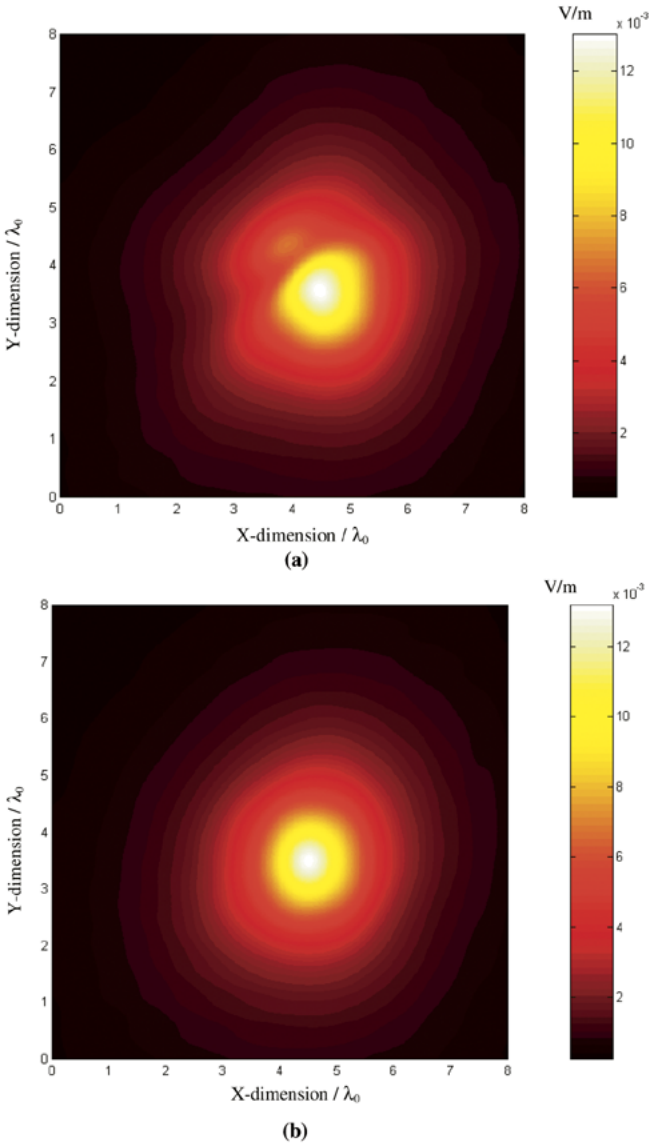

Fig. 6. Scattered electric field above a flat ground at $z = 0.5\lambda_0$ due to just the spheroid alone. (a) Originally buried under the flat ground and nearby the cylinder as in Fig. 5(a). (b) Originally buried under the flat ground as a single object (no nearby cylinder). H-polarization.

in the spheroid signature. The magnitude decrease observed in Fig. 5(d) compared with (c) is due to the larger burial depth of the spheroid in the former case that caused more attenuation in the transmitting waves.

In Fig. 6(a), the spheroid is buried near the horizontal cylinder but beneath a flat ground instead of the rough ground (i.e. without the effect of ground roughness). In Fig. 6(b), the spheroid is buried alone as a single object beneath the flat ground (i.e. without the effect of the cylinder or the ground roughness). Comparing Fig. 6(a) with (b) show the distortion level in the spheroid signature due to only the presence of the cylinder. On the other hand, comparing Fig. 5(c) [or 5(d)] with Fig. 6(a) show the distortion level due to the ground roughness. However, comparing Fig. 5(c) [or Fig. 5(d)] with Fig. 6(b) show the distortion level due to both the ground roughness and the nearby cylinder. The signature in Fig. 5(c) is slightly different from Fig. 6(a) because of the small ground roughness

considered in this case, however, the difference increases in Fig. 5(d) due to the increase in the ground rms height. When the clutter is removed by subtraction using only the magnitude of the fields (i.e. with ignoring the phase), the spheroid signature becomes more distorted (not presented).

Using the SDFMM code required approximately 850-MB computer memory, 25 CPU minutes to fill the near field matrix, 23 CPU minutes to calculate the near scattered fields, and 4.6 CPU hours to achieve relative error equal to 10^{-5} for the transpose free quasi-minimal residual (TFQMR) iterative solver [34]. The computations for the rough ground are dominating the process in all simulations, therefore, the CPU time and computer memory are slightly different from case to case. Note that the ground dimensions are the same for all cases. The computations were conducted using the Compaq Alpha Server (GS140 EV6) with 667 MHz clock speed.

IV. Conclusion

The 3-D scattering problem of multiple dielectric shallow objects buried beneath two-dimensional random rough ground is formulated. The parametric investigations show the significant effect of the separation distance between objects on the target signature. In addition, as the ground roughness increases, the target signature becomes more distorted. These results imply the large possibility of a false alarm in detecting the target when it is buried nearby a clutter item.

Acknowledgment

This work was conducted using the Northeastern University Advanced Scientific Computation Center.

References

[1] G. Zhang and L. Tsang, "Application of angular correlation function of clutter scattering and correlation imaging in target detection," *IEEE Trans. Geosci. Remote Sensing*, vol. 36, pp. 1485–1493, Sept. 1998.

[2] K. O'Neil, "Discrimination of UXO in soil using broadband polarimetric GPR backscatter," *IEEE Trans. Geosci. Remote Sensing*, vol. 39, pp. 356–367, Sept. 2001.

[3] N. Geng, A. Sullivan, and L. Carin, "Multilevel fast-multipole algorithm for scattering from conducting targets above or embedded in a lossy half space," *IEEE Trans. Geosci. Remote Sensing*, vol. 38, pp. 1561–1573, July 2000.

[4] Z. Xiong and A. C. Tripp, "3-D electromagnetic modeling for near-surface targets using integral equations," *Geophys.*, vol. 62, no. 4, pp. 1097–1106, Aug. 1997.

[5] G. S. Smith and L. E. Rickard Peterson, "On the use of evanescent electromagnetic waves in the detection and identification of objects buried in lossy soil," *IEEE Trans. Antennas Propagat.*, vol. 48, pp. 1295–1300, Sept. 2000.

[6] L. Gürel and U. Oğuz, "Three-dimensional FDTD modeling of a ground-penetrating radar," *IEEE Trans. Geosci. Remote Sensing*, vol. 38, pp. 1513–1521, July 2000.

[7] R. T. Ling and P. Y. Ufimtsev, "Scattering of electromagnetic waves by a metallic object partially immersed in a semi-infinite dielectric medium," *IEEE Trans. Antennas Propagat.*, vol. 49, pp. 223–233, Feb. 2001.

[8] J. T. Johnson, "A study of the four-path model for scattering from an object above a halfspace," *Microwave Opt. Tech. Lett.*, pp. 130–134, July 2001.

[9] A. Sullivan, R. Damarla, N. Geng, Y. Dong, and L. Carin, "Ultrawide-band synthetic aperture radar for detection of unexploded ordnance: modeling and measurements," *IEEE Trans. Antennas Propagat.*, vol. 48, pp. 1306–1315, Sept. 2000.

[10] Y. Xu, R. M. Narayanan, X. Xu, and J. O. Curtis, "Polarimetric processing of coherent random noise radar data for buried object detection," *IEEE Trans. Geosci. Remote Sensing*, vol. 39, pp. 467–478, Mar. 2001.

[11] S. Nag and L. Peters Jr., "Radar images of penetrable targets generated from ramp profile functions," *IEEE Trans. Antennas Propagat.*, vol. 49, pp. 32–40, Jan. 2001.

[12] T. Dogaru, L. Collins, and L. Carin, "Optimal time-domain detection of a deterministic target buried under a randomly rough interface," *IEEE Trans. Antennas Propagat.*, vol. 49, pp. 313–326, Mar. 2001.

[13] K. O'Neill, "Broadband bistatic coherent and incoherent detection of buried objects beneath randomly rough surfaces," *IEEE Trans. Geosci. Remote Sensing*, vol. 38, pp. 891–898, Mar. 2000.

[14] G. Zhang, L. Tsang, and Y. Kuga, "The angular correlation function of wave scattering by a buried object embedded in random discrete scatterers under a random rough surface," *Microwave Opt. Technol. Lett.*, vol. 14, no. 3, pp. 144–151, Feb. 1997.

[15] A. Madrazo and M. Nieto-Vesperinas, "Scattering of light and other electromagnetic waves from a body buried beneath a highly rough random surface," *J. Opt. Soc. Am. A*, vol. 14, no. 8, pp. 1859–1866, Aug. 1997.

[16] K. O'Neill, R. F. Lussky Jr., and K. D. Paulsen, "Scattering from a metallic object embedded near the randomly rough surface of a lossy dielectric," *IEEE Trans. Geosci. Remote Sensing*, vol. 34, pp. 367–376, Mar. 1996.

[17] G. Zhang, L. Tsang, and K. Pak, "Angular correlation function and scattering coefficient of electromagnetic waves scattered by a buried object under a two-dimensional rough surface," *J. Opt. Soc. Am. A*, vol. 15, no. 12, pp. 2995–3002, Dec. 1998.

[18] J. T. Johnson and R. J. Burkholder, "Coupled canonical grid/discrete dipole approach for computing scattering from objects above or below a rough interface," *IEEE Trans. Geosci. Remote Sensing*, vol. 39, pp. 1214–1220, June 2001.

[19] J. T. Johnson, "A numerical study of scattering from an object above a rough surface," *IEEE Trans. Antennas Propagat.*, vol. 48, pp. 1361–1367, Oct. 2002.

[20] M. El-Shenawee, C. Rappaport, E. Miller, and M. Silevitch, "3-D subsurface analysis of electromagnetic scattering from penetrable/PEC objects buried under rough surfaces: use of the steepest descent fast multipole method (SDFMM)," *IEEE Trans. Geosci. Remote Sensing*, vol. 39, pp. 1174–1182, June 2001.

[21] M. El-Shenawee, C. Rappaport, and M. Silevitch, "Monte Carlo simulations of electromagnetic wave scattering from random rough surface with 3-D penetrable buried object: mine detection application using the SDFMM," *J. Opt. Soc. Am. A*, Dec. 2001.

[22] I. J. Won, D. A. Keiswetter, and T. H. Bell, "Electromagnetic induction spectroscopy for clearing landmines," *IEEE Trans. Geosci. Remote Sensing*, vol. 39, pp. 703–709, Apr. 2001.

[23] V. Jandhyala, "Fast Multilevel Algorithms for the Efficient Electromagnetic Analysis of Quasi-Planar Structures," Ph.D. dissertation, Dept. Elec. Comput. Eng., Univ. Illinois at Urbana-Champaign, , 1998.

[24] V. Jandhyala, B. Shanker, E. Michielssen, and W. C. Chew, "A fast algorithm for the analysis of scattering by dielectric rough surfaces," *J. Opt. Soc. Am. A*, vol. 15, no. 7, pp. 1877–1885, July 1998.

[25] M. El-Shenawee, V. Jandhyala, E. Michielssen, and W. C. Chew, "The steepest descent fast multipole method (SDFMM) for solving combined field integral equation pertinent to rough surface scattering," in *Proc. '99 IEEE APS/URSI Conf.*, Orlando, FL, July 1999, pp. 534–537.

[26] L. Medgyesi-Mitschang, J. Putnam, and M. Gedera, "Generalized method of moments for three-dimensional penetrable scatterers," *J. Opt. Soc. Am. A*, vol. 11, no. 4, pp. 1383–1398, Apr. 1994.

[27] S. M. Rao, D. R. Wilton, and A. W. Glisson, "Electromagnetic scattering by surfaces of arbitrary shape," *IEEE Trans. Antennas Propagat.*, vol. AP30, pp. 409–418, May 1982.

[28] P. Tran and A. A. Maradudin, "Scattering of a scalar beam from a two-dimensional randomly rough hard wall: enhanced backscatter," *Phy. Rev. B*, vol. 45, no. 7, pp. 3936–3939, Feb. 1992.

[29] C. Rappaport, S. Azevedo, T. Rosenbury, J. Gough, and A. Dean, "Detecting antipersonnel mines with a handheld parabolic reflector transmitter/multistatic receiver impulse GPR," in *Proc. '2000 UXO/Countermine Forum*, May 2000, pp. 1–8.

[30] C. Rappaport, S. Azevedo, T. Rosenbury, and J. Gough, "Handheld forward-looking focused array mine detection with plane wave excitation," in *Proc. SPIE Aerosense Conf.*, Orlando, FL, Apr. 2000, pp. 1118–1126.
[31] N. Garcia and E. Stoll, "Monte Carlo calculation for electromagnetic-wave scattering from random rough surfaces," *Phy. Rev. Let.*, vol. 52, no. 20, pp. 1798–1801, May 1984.
[32] "US Army Corp. of Eng., Waterways Experimental Station Data Rep.,", 1996.
[33] C. A. Balanis, *Advanced Engineering Electromagnetics*. New York: Wiley, 1989, ch. 6, pp. 254–309.
[34] R. W. Freund, "A transpose-free quasiminimal residual algorithm for nonhermitian linear systems," *SIAM J. Sci. Comput.*, vol. 14, no. 2, pp. 470–482, Mar. 1993.

Magda El-Shenawee (M'91–SM'02) received the B.S. and M.S. degrees in electrical engineering from Assiut University, Assiut, Egypt, and the Ph.D. degree in electrical engineering from the University of Nebraska-Lincoln, in 1991.

In 1992, she worked as a Research Associate in the Center for Electro-Optics at the University of Nebraska, where she focused on the problem of enhanced backscatter phenomena. In 1994, she worked as a Research Associate at the National Research Center, Cairo, Egypt, and in 1997, she worked as a Visiting Scholar at the University of Illinois at Urbana-Champaign. In 1999, she joined the Multidisciplinary University Research Initiative team (MURI) at Northeastern University, Boston. Currently, she is an Assistant Professor with the Department of Electrical Engineering, University of Arkansas, Fayetteville. Her research interests include rough surface scattering, computational electromagnetics, subsurface sensing of buried objects, breast cancer modeling, numerical methods, and micro-strip circuits.

Dr. El-Shenawee is a Member of Eta Kappa Nu Electrical Engineering Honor Society.